Article:

Zhao, Xing orcid.org/0000-0003-4000-0446, Wang, Weiyu and Niu, Shuangxia (2022) Reconstructing Saliency Effect in 12/10 DC Vernier Reluctance Machine for Position-Sensorless Drive Aerospace Starter Generator Application. IEEE Transactions on Energy Conversion. 9757862. ISSN 0885-8969

https://doi.org/10.1109/TEC.2022.3167551

Reconstructing Saliency Effect in 12/10 DC Vernier Reluctance Machine for Position-Sensorless Drive Aerospace Starter Generator Application

Xing Zhao, *Member, IEEE*, Weiyu Wang, Shuangxia Niu, *Senior Member, IEEE,* W.N. Fu

***Abstract*- DC-Excited vernier reluctance machine (DC-VRM) using a 12-slot/10-pole-pair design, exhibits the advantages of small torque ripple and low cogging torque due to the inherent commentary characteristic. However, the inherent saliency is canceled out by a 12/10 pole combination of machine design driven by a traditional three-phase inverter. As a result, the sensorless operation in zero/low-speed regions becomes difficult because the position estimation methods using self-inductance detection cannot be applied. To tackle this problem, we first analyzed the saliency annihilation phenomenon through Fourier analysis that the odd-order harmonics in self-inductance are canceled. Moreover, reconstructing saliency method is proposed by splitting a phase winding into two sub-phase coils and using parallel H-bridge converters to supply sub-phase coils and achieve sensorless drive. Through this method, the saliency effect is recovered in self-inductance, thereby pulse injection sensorless drive can be applied. The constructed 12/10 DC-VRM sensorless drive shows good fault-tolerant ability and can be applied in safety-critical industry applications such as aerospace propulsion. Analysis and experiments are performed in the initial position detection, start-up and free-running stages to verify the feasibility of the proposed solution. A sector estimation accurate to 6° can be achieved.**

***Index Terms*— DC Vernier Reluctance Machine (DC-VRM), integrated starter/generator (ISG), reconstructing saliency effect, aerospace applications.**

I. Introduction

With the increasing concern for environmental protection and energy-saving, the research of integrated starter/generator (ISG) in more electrical aircraft applications has attracted more attention [1-3]. Electrical machines, as the key components of the ISG system, are exposed to new challenges of higher power density, efficiency, reliability, etc. Permanent magnet materials suffer from the risk of demagnetization in high temperatures [4-5], thereby developing reluctance machines has been a hot topic in recent years [6-8].

Manuscript received Oct 05, 2021; revised Feb 02, 2022; accepted Apr 09, 2022. This work was supported by the National Natural Science Foundation of China under Project 52077187 and in part by the Research Grant Council of the Hong Kong Government under Project PolyU 152143/18E and PolyU 152109/20E. (Corresponding author: Shuangxia Niu)

Xing Zhao is with the Department of Electronic Engineering, University of York, United Kingdom. (e-mail: xing.zhao@york.ac.uk)

Weiyu Wang and Shuangxia Niu are with the Department of Electrical Engineering, The Hong Kong Polytechnic University, Hong Kong, China. (e-mail: weiyu.wang@connect.polyu.hk; eesxniu@polyu.edu.hk)

W.N. Fu is with Shenzhen Institutes of Advanced Technology, Chinese Academy of Sciences, China. (e-mail: wn.fu@siat.ac.cn)

Reluctance machines using the doubly salient structure is a potential solution, due to the simple and robust structure. One typical candidate is switched reluctance machine (SRM), which has been well studied in literature over the last twenty years associated with analytical modeling, numerical design, control strategies [9-11], etc. However, SRM suffers from a large torque ripple due to the half-cycle conducting principle, leading to severe mechanical vibration and noise [12-13]. Doubly-fed doubly salient machine (DF-DSM) shares the same slot pole design as SRM but with extra distributed DC field coils in the stator, which enables it to operate in the whole electrical period and be driven by an inverter package. However, its torque ripple is still unacceptable due to the unbalanced magnetic circuit between phases and rich even-order flux harmonics [14-15].

Recently, a new type of doubly salient reluctance machine is proposed, namely variable flux reluctance machine (VFRM), which shares a similar configuration with DF-DSM, while the DC field coils are uniformly distributed in the stator core [16]. Benefiting from the uniform DC field excitation, VFRM can essentially achieve a balanced magnetic circuit between phases. Further, it is revealed that the working principle of VFRM can be illustrated by the emerging flux modulation theory [17-21]. Accordingly, it can be referred to as a special type of DC-excited Vernier reluctance machine (DC-VRM). Compared to SRM and DF-DSM counterparts, more slot pole combinations can be used in DC-VRM, especially the unit machine design with even-order rotor pole pair, which contributes to small torque ripple due to the elimination of even-order flux harmonics and the minimum cogging torque. Therefore, from the perspective of noise and vibration, DC-VRM can be a better rare-earth-free solution to be applied as aerospace ISG.

The sensorless operation can further simplify the drive circuit of electrical machines and improve system reliability, which attracted much attention in academia and industry [22-24]. For reluctance machines with doubly salient structures, the air gap permeance changes with rotor position periodically, leading to the variation of phase inductance at the same time. This gives the advantage of a sensorless operation based on those position estimation methods by detecting winding inductances. For SRM, many research works have been reported in terms of sensorless operation based on the indirect inductance detection method [25-26]. At the early stage, a linear model of SRM inductance is developed to divide the three-phase inductance sector for the low-speed sensorless operation [27]. To improve the detection accuracy, an improved non-conducting phase pulse injection method is proposed by detecting high linearity

This article has been accepted for publication in a future issue of this journal, but has not been fully edited. Content may change prior to final publication. Citation information: DOI 10.1109/TEC.2022.3167551, IEEE Transactions on Energy Conversion

characteristics of the inductance drop interval in the four quadrants [28]. A dual-threshold inductance detection method for non-conducting phase current is proposed [29]. The commutation angle can be regulated by adjusting the current threshold to meet the requirements of the load torque condition. In [30], the phase inductance is calculated by measuring the time when the capacitor charging reaches the maximum current in the bootstrap circuit to determine the initial conduction phase of the machine and the initial position of the rotor, while the start-up operation control cannot be realized. A simple sensorless drive method using the Wien bridge is proposed by H. Moradi and E. Afjei to detect the rotor position at a standstill and low speeds in switched reluctance motor [31]. Furthermore, an optimized Hays bridge is applied and adjusted to achieve a balanced condition in an unaligned position when reaching the minimum inductance point. This method provides simplicity in the implementation and tuning flexibility [32]. A reconstruction method of unsaturated inductance is proposed in [33], in which the unsaturated inductance is fitted as a second-order function of incremental inductance and chopping current reference. For DF-DSM, the inductances can be indirectly detected by phase-induced voltages during the DC excitation building stage [34], but this method is only suitable for initial position detection. For the acceleration stage, the pulse injection method by alternately injecting detection pulses and acceleration pulses in sequence has been proven effective [35].

However, the inherent serious problem of torque ripple in SRM and DF-DSM leads to the mechanical vibration of the rotor, which increases the difficulty of accurate position estimation in a sensorless control system, thus limiting their industry application. DC-VRM can achieve low torque ripple with specific slot pole combinations. Therefore, the development of DC-VRM sensorless operation can create a solution that combines sensorless merits and low torque ripple performance. To achieve this goal, one key issue needs to be addressed. That is, for DC-VRM using even rotor pole pair in unit machine design, the saliency effect of the machine is annihilated, hence those advanced sensorless control methods using self-inductance detection cannot be applied. In this paper, a parallel sensorless drive method is proposed for DC-VRM. The key is to use a parallel H-bridge converter to reconstruct the machine saliency for rotor position estimation by detecting inductances. Benefiting from the reconstructed saliency and inherent low torque ripple character of DC-VRM, a high-performance robust sensorless operation can be realized, which has good potential to be applied as aerospace ISG. The arrangements of this paper are as follows. In Section II, both the saliency annihilation phenomenon and the saliency reconstructing method are analyzed. The parallel drive structure through reconstructing saliency effect, as well as the mathematical model of DC-VRM, are introduced. In Section III, the self-inductance and mutual inductance characteristics, as well as their effect on sensorless operation are analyzed. In Section IV, a position estimation method by current pulse injection and inductance detection is employed for sensorless operation. In Section V, the prototype and test bench is built, and experimental results are presented. Finally, some conclusions are drawn.

II. Configuration of DC-VRM Drive System

A. Configuration of DC-VRM

As shown in Fig .1, ISG can work as a starter during the startup process and operates as a generator to recycle the energy from the aerospace engine, thereby the total weight, volume and costs can be decreased through the integrated machine design. The structure of the 12/10 DC-VRM to be studied is provided in Fig.2. The DC field coils are wound on each stator tooth, and the directions of two adjacent DC field coils are opposite. All the DC field coils are connected in series to form one single DC field winding. The AC armature coils are wound on each stator tooth as well. The parameters of the prototype machine are listed in Table I.

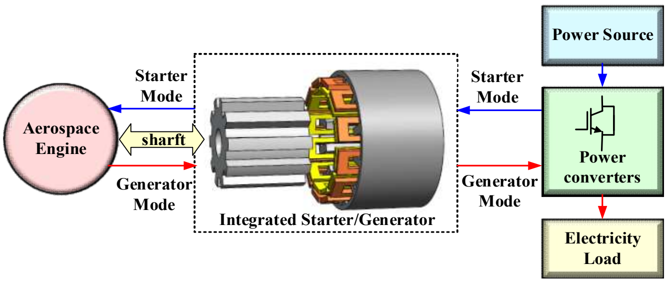

Fig. 1. Aerospace integrated starter and generator system.

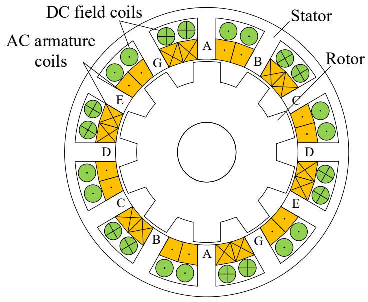

Fig. 2. Structure of 12/10 DC-VRM.

TABLE I
SPECIFIC PARAMETERS FOR THE DC-VRM

Symbol	Parameter	Unit	Value
d_{so}	Outer diameter of stator	mm	130
d_{si}	Inner diameter of stator	mm	90
d_{ro}	Outer diameter of rotor	mm	89
d_{ri}	Inner diameter of rotor	mm	60
α_s	Stator pole arc	°	12
α_r	Rotor pole arc	°	18
δ	Air gap length	mm	0.5
l	Stack length	mm	80
N_{dc}	Turns of each DC coil	-	48
N_{ac}	Turns of each AC coil	-	48
R	Sub-phase winding resistance	Ω	0.7
R_f	Field winding resistance	Ω	4.2

B. Fourier Analysis of Saliency Annihilation Phenomenon in Traditional Drive Topology

Fig .3 shows the traditional three-phase inverter drive topology of 12/10 DC-VRM. Two sets of armature coils that have 180° phase differences are reversely cascaded to form a single-phase winding. For example, phase U is formed by a reverse series connection of phases A and D.

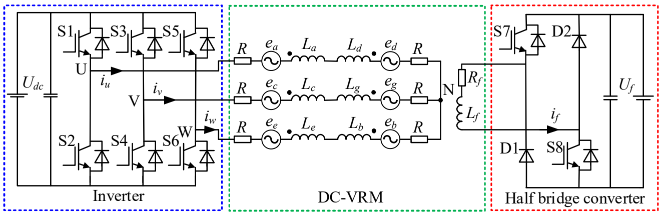

Fig .3. Traditional three-phase inverter drive topology for 12/10 DC-VRM.

As sub-phase A and D have 180° phase differences, the Fourier expansion of their self-inductance can be expressed as

$$L_a = L_{dc} + \sum L_n \sin(n\omega t + \theta_n) \quad , \quad n = 1, 2, 3 \ldots . \tag{1}$$

$$L_d = L_{dc} + \sum L_n \sin(n\omega t + n\pi + \theta_n) \quad , \quad n = 1, 2, 3 \ldots . \tag{2}$$

where L_a and L_d are the self-inductances of sub-phases A and D. L_{dc} is the DC self-inductance component. L_n is the amplitude of the nth harmonics, ω is the electrical angular velocity, θ_n is the initial phase angle of nth harmonics. The Fourier expansion of the self-inductance of phase U L_U can be regarded as the composition of sub-phases A and D.

$$L_U = L_a + L_d = 2L_{dc} + 2\sum L_n \sin(n\omega t + \theta_n) \quad , \quad n = 2, 4, 6 \ldots . \tag{3}$$

As shown in equation (3), a saliency annihilation phenomenon can be found in L_U. The odd-order harmonics including the fundamental component are canceled when they are superimposed. As a doubly salient machine, the saliency effect mainly exists in the fundamental harmonic component. This phenomenon constrains the application of saliency tracking sensorless drive methods.

To further describe the saliency annihilation phenomenon, Fig. 4 shows the self-inductances of phases A, D and U and their harmonics distributions calculated by the finite element simulation. Driven by the traditional three-phase inverter, the phase self-inductance is a superposition of that of two sub-phases having a 180° phase difference. Therefore, all the odd-order harmonic inductances are canceled, when the bias component and the odd-number harmonic inductances are superimposed. It is clear to see that the self-inductance amplitude of phase U does not change significantly with the rotor position, only fluctuating within the range of 0.2mH approximately, which means the saliency of the machine is annihilated, regardless of its salient-pole structure and associated variable self-inductance of each sub-phase group. As is well known, machine saliency has a significant effect on sensorless operation, especially for the zero and low-speed ranges. However, the saliency is annihilated in the traditional three-phase inverter-based DC-VRM drive system.

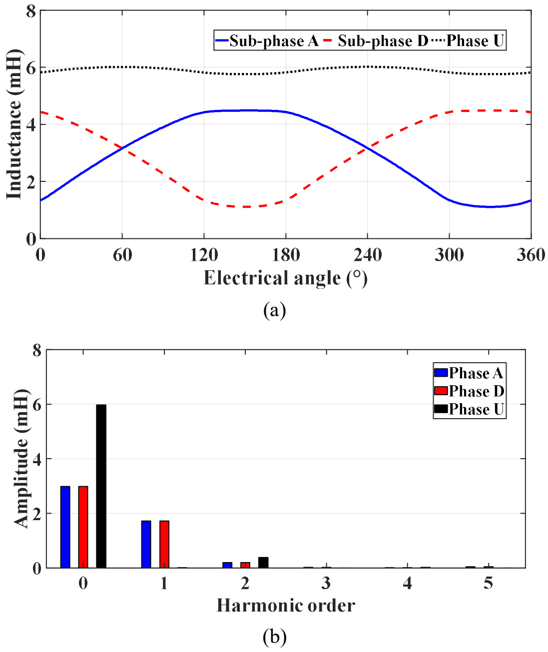

Fig. 4. (a) Phase inductances of A, D and U. (b) Harmonics distributions.

C. Reconstructing Saliency Effect by Parallel H-Bridge-Converter Sensorless Drive System

To reconstruct the saliency effect of DC-VRM for position sensorless operation, a parallel H-bridge drive configuration is proposed in Fig .5. It can be seen that those reversely connected three-phase armature windings can be separated as six sub-phase groups (A, B, C, D, E, G) and each sub-phase can be independently excited by an H-bridge converter. In this way, the inherent saliency effect of each sub-phase winding can be utilized for low-speed sensorless operation.

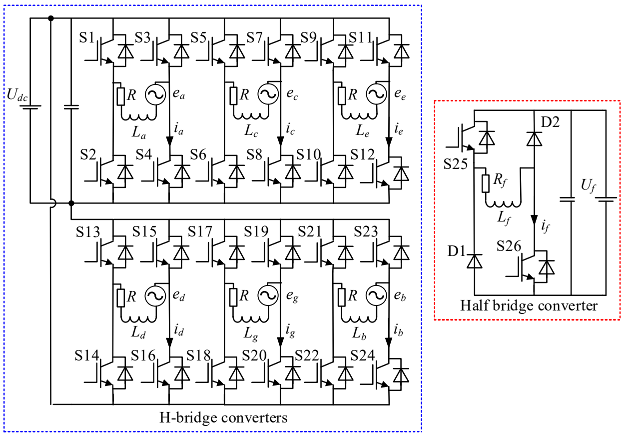

Fig. 5. H-bridge drive structure of DC-VRM.

The advantages of the proposed parallel H-bridge-converter based sensorless drive system can be summarized as

(1) This drive system keeps the complementary electromagnetic characteristic of the 12/10 DC-VRM in reducing torque ripple by eliminating even-order flux harmonics.
(2) The saliency effect of sub-phase windings can be released. Within an electrical period, the variable self-inductance curves of six sub-phase windings with a uniform phase difference of 60°, can be utilized to estimate the rotor position.
(3) Using a parallel H-bridge converter allows each sub-phase to be independently excited, thus the effect of winding mutual inductance on the rotor position estimation can be minimized, which can improve the accuracy of the estimated position.
(4) The H-bridge drive structure shows a significant advantage in fault tolerance to improve system reliability, which is quite suitable for aerospace applications.

D. Mathematical Model of 12/10 DC-VRM

The parallel H-bridge drive enables each sub-phase winding to be independently controlled, and the current, inductance and torque equations of DC-VRM can be expressed as

$$I=[i_a \quad i_b \quad i_c \quad i_d \quad i_e \quad i_g \quad i_f]^T \tag{4}$$

$$L=\begin{bmatrix} L_a & L_{ab} & L_{ac} & L_{ad} & L_{ae} & L_{ag} & L_{af} \\ L_{ab} & L_b & L_{bc} & L_{bd} & L_{be} & L_{bg} & L_{bf} \\ L_{ac} & L_{bc} & L_c & L_{cd} & L_{ce} & L_{cg} & L_{cf} \\ L_{ad} & L_{bd} & L_{cd} & L_d & L_{de} & L_{dg} & L_{df} \\ L_{ae} & L_{be} & L_{ce} & L_{de} & L_e & L_{eg} & L_{ef} \\ L_{ag} & L_{bg} & L_{cg} & L_{dg} & L_{eg} & L_g & L_{gf} \\ L_{af} & L_{bf} & L_{cf} & L_{df} & L_{ef} & L_{gf} & L_f \end{bmatrix} \tag{5}$$

$$T=\frac{1}{2}I^T\frac{dL}{d\theta}I \tag{6}$$

where I is the current matrix, i_a, i_b, i_c, i_d, i_e and i_g are the sub-phase currents, i_f is the field current, L is the inductance matrix, L_{af}, L_{bf}, L_{cf}, L_{df}, L_{ef} and L_{gf} are the mutual inductances between sub-phase windings and the field winding, L_a, L_b, L_c, L_d, L_e and L_g are the self-inductances of sub-phases, L_{ab}, L_{ac}, L_{ad}, L_{ae}, L_{ag}, L_{bc}, L_{bd}, L_{be}, L_{bg}, L_{cd}, L_{ce}, L_{cg}, L_{de}, L_{dg} and L_{eg} are the mutual inductances between sub-phases, L_f is the self-inductance of the field winding, T is the total torque, θ is the electrical angle.

Taking sub-phase A as an example, the torque components under current excitation can be expanded as

$$T_a=i_ai_f\frac{dL_{af}}{d\theta}+\frac{1}{2}i_a^2\frac{dL_a}{d\theta}+\frac{1}{2}i_f^2\frac{dL_f}{d\theta}+T_{am} \tag{7}$$

The first term is the major component of the excitation torque produced by the mutual inductance between DC field winding and the sub-phase winding. The second term is the reluctance torque produced by variation of sub-phase self-inductance. Due to bipolar current excitation, the average reluctance torque in the whole electrical period is zero. The third term is the cogging torque produced by DC field winding. As L_f keeps constant in the whole electrical period, the cogging torque can be neglected. T_{am} is the torque component produced by mutual inductances between sub-phase windings and can be expanded as

$$T_{am}=\frac{1}{2}i_a(i_b\frac{dL_{ab}}{d\theta}+i_c\frac{dL_{ac}}{d\theta}+i_d\frac{dL_{ad}}{d\theta}+i_e\frac{dL_{ae}}{d\theta}+i_g\frac{dL_{ag}}{d\theta}) \tag{8}$$

III. Inductance Characteristics

A. Self-inductance Characteristics

For reluctance machines with doubly saliency structures, the self-inductance equation is described as

$$L(\theta)=\frac{N_{ac}^2\mu S}{l} \tag{9}$$

where S is the cross-sectional area of the stator poles and rotor poles overlapping, μ is the permeability, l is the flux path length. The sub-phase self-inductance model is shown in Fig .6. The initial position is defined as the position where the rotor tooth and stator tooth begin to mesh. With the increase in the overlap area of the rotor tooth and the stator tooth, the sub-phase self-inductance increases proportionally. When the rotor tooth and stator tooth begin to mesh completely, the sub-phase self-inductance reaches its peak value. As α_s is designed smaller than α_r, a flat top and bottom in self-inductance are acquired.

Through finite element analysis, the self-inductance curves of six sub-phases are shown in Fig. 7. The amplitudes of each self-inductance curve are equal, and the phase angle differences between two adjacent self-inductance curves are 60°. The inherent saliency is released through H-bridge sensorless drive structure, and the symmetry of these self-inductance curves can guarantee the accuracy of position estimation.

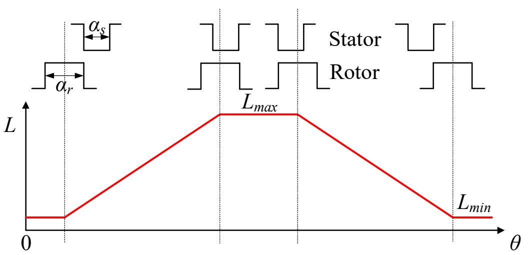

Fig. 6. Sub-phase self-inductance model.

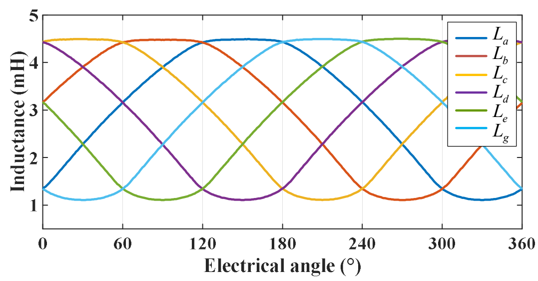

Fig. 7. Sub-phase self-inductance curves.

B. Mutual Inductance Characteristics

In DC-VRM, two kinds of mutual inductance exist. The first one is the mutual inductance between field winding and sub-phase winding. In each stator tooth, field winding and sub-phase winding have similar magnetic circuits. Taking sub-phase A as an example, L_{af} and L_a have the same phase, and the amplitude is related to the turn ratio n of the field winding and sub-phase winding, and the relationship can be marked as

$$L_{af}=\frac{N_{dc}}{N_{ac}}L_a=nL_a \tag{10}$$

Another mutual inductance exists between sub-phase groups. The flux distributions at four typical rotor positions are revealed in Fig .8. When sub-phase A is in the aligned or half-aligned positions, the coupling relationships between sub-phase A and the other sub-phases are seen in Fig .8(a), Fig .8(b) and Fig .8(c). The amplitudes of the mutual inductance are related to the meshing degree of the stator teeth and rotor teeth. By contrast, when sub-phase A is in a completely unaligned position shown in Fig .8(d), its coupling degrees with the other sub-phases are weak. Since the magnetic circuit between phases A and D is longer and the cross-sectional area of the magnetic circuit is small, L_{ad} is small with a slight fluctuation in the whole period.

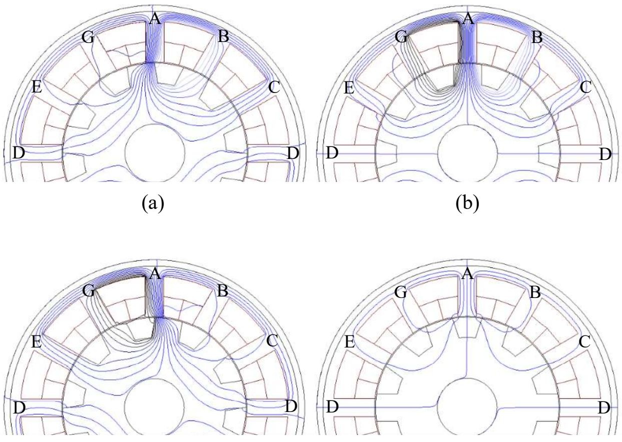

Fig. 8. The mutual inductances between sub-phases at different rotor positions. (a) 60°. (b) 150°. (c) 240°. (d) 330°.

The mutual inductance curves between sub-phase A and the other sub-phases in a whole electrical period are shown in Fig .9. The unneglectable fluctuations are seen in L_{ab}, L_{ac}, L_{ae} and L_{ag}. The inherent mutual inductance complicates the inductance model, producing a negative effect on inductance detection-based sensorless control. This influence can be avoided by using the parallel sensorless drive method as revealed in the next sector.

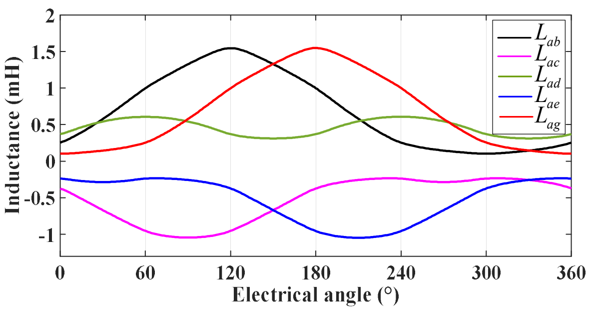

Fig. 9. Mutual inductance between sub-phases.

IV. Sequential Pulse Injection Sensorless Drive Avoiding Mutual Inductance Influence

Pulse injection sensorless drive method has the advantages of strong reliability and no need for additional circuits, which is suitable for low-speed sensorless control in electrical machines having a saliency effect. Using a parallel H-bridge drive structure in DC-VRM, the saliency of the sub-phase can be reconstructed. This enables the pulse injection method for position estimation. Moreover, to avoid the influence of mutual inductance between sub-phases on the position estimation accuracy. A sequential pulse injection can be applied, benefiting from the independent current control feature using the parallel H-bridge drive system, which will be presented in detail in this section.

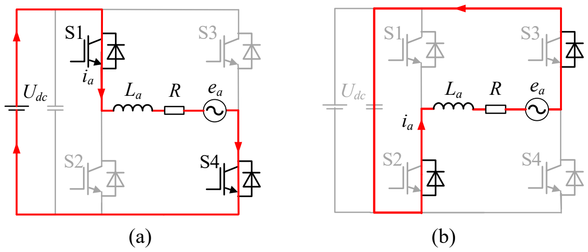

Fig. 10. Equivalent circuit. (a) Pulse injection. (b) Demagnetization.

A. Sequential Pulse Injection based Sensorless Operation

Fig .10(a) shows the schematic diagram of pulse injection in sub-phase A. A short detection voltage pulse is injected by switching on power transistors S1 and S4. i_a increases sharply during this stage. When the detection pulse injection is finished, the peak point value of i_a is recorded. Meanwhile, S1 and S4 are switched off to enter the demagnetization process which is shown in Fig .10(b). In this process, i_a decreases to 0. From Fig. 10(a), The equivalent voltage equation for sub-phase under pulse injection can be described as

$$U_{dc}=L_a\frac{di_a}{dt}+e_a+i_aR \tag{11}$$

Where e_a is the back-electromotive force (back-EMF) of sub-phase A. In the initial detection and acceleration stage, the motor speed is zero or quite small, and back-EMF can be ignored. In addition, the detection pulse duration is short and the resultant current amplitude is small, the voltage drop on the winding can also be neglected. Considering the short duration of the detection pulse, it can be considered that the sub-phase winding current rises linearly during this period. The measured sub-phase self-inductance equation can be expressed as (8).

$$L_a=\frac{U_{dc}\Delta t}{I_a} \tag{12}$$

where Δt is the detection pulse width. I_a, I_b, I_c, I_d, I_e and I_g are defined as the peak point current values of sub-phases. The relationship between electrical angle, sub-phase self-inductance, sub-phase peak currents and rotor electrical sector are listed in Table II. The information on sub-phase self-inductance can be indirectly acquired by calculating the peak point of sub-phase currents. By comparing self-inductance values, the rotor

This article has been accepted for publication in a future issue of this journal, but has not been fully edited. Content may change prior to final publication. Citation information: DOI 10.1109/TEC.2022.3167551, IEEE Transactions on Energy Conversion

electrical period is divided into six sectors based on the conduction mode.

TABLE II
RELATION BETWEEN ELECTRICAL ANGLE, SUB-PHASE SELF-INDUCTANCES, SUB-PHASE PEAK CURRENTS AND ROTOR SECTOR

Electrical Angle	Relation of sub-phase self-inductances	Relation of sub-phase peak currents	Rotor Sector
0-30	$L_c>L_d>L_b>L_e>L_a>L_g$	$I_c<I_d<I_b<I_e<I_a<I_g$	I
30-60	$L_c>L_b>L_d>L_a>L_e>L_g$	$I_c<I_b<I_d<I_a<I_e<I_g$	
60-90	$L_b>L_c>L_a>L_d>L_g>L_e$	$I_b<I_c<I_a<I_d<I_g<I_e$	II
90-120	$L_b>L_a>L_a>L_g>L_d>L_e$	$I_b<I_a<I_a<I_g<I_d<I_e$	
120-150	$L_a>L_b>L_g>L_c>L_e>L_d$	$I_a<I_b<I_g<I_c<I_e<I_d$	III
150-180	$L_a>L_g>L_b>L_e>L_c>L_d$	$I_a<I_g<I_b<I_e<I_c<I_d$	
180-210	$L_g>L_a>L_e>L_b>L_d>L_c$	$I_g<I_a<I_e<I_b<I_d<I_c$	IV
210-240	$L_g>L_e>L_a>L_d>L_b>L_c$	$I_g<I_e<I_a<I_d<I_b<I_c$	
240-270	$L_e>L_g>L_d>L_a>L_c>L_b$	$I_e<I_g<I_d<I_a<I_c<I_b$	V
270-300	$L_e>L_d>L_g>L_c>L_a>L_b$	$I_e<I_d<I_g<I_c<I_a<I_b$	
300-330	$L_d>L_e>L_c>L_g>L_b>L_a$	$I_d<I_e<I_c<I_g<I_b<I_a$	VI
330-360	$L_d>L_c>L_e>L_b>L_g>L_a$	$I_d<I_c<I_e<I_b<I_g<I_a$	

Fig. 11 illustrates the schematic diagram of initial position detection and acceleration. During the position detection period (t_1 to t_2), to avoid the influence of mutual inductance between the sub-phases, the H-bridge sensorless control system is introduced to control each sub-phase independently. The detection pulses of the next sub-phase are injected after the previous sub-phase has completed the demagnetization period. Consequently, by injecting detection pulses in each sub-phase in sequence, the accuracy of position estimation is not affected by the mutual inductance influence between the sub-phases.

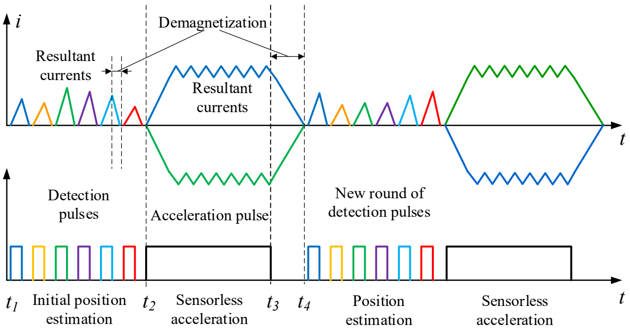

Fig. 11. Schematic diagram of initial position detection and acceleration.

The rotor position can be estimated by comparing the peak values of resultant currents in each sub-phase winding. Then the conduction phases of the DC-VRM are determined, and further acceleration pulses are injected during the period between t_2 and t_3. To continue to speed up the machine, the detection pulses and acceleration pulses are injected alternately for position detection and acceleration, respectively. After each sub-phase completes the demagnetization between t_3 and t_4, a new round of detection pulses is injected from t_4.

The conduction phases of the DC-VRM are determined by the mutual inductance between field winding and sub-phase windings which can be found in Fig .12. According to the principle of DC-VRM, the positive and negative direction currents flow during the rising stage and falling stage of the mutual inductance between the field winding and sub-phase windings, respectively. This trapezoidal inductance feature can effectively avoid the direct current jump from positive to negative, and reduce the torque ripples during commutation.

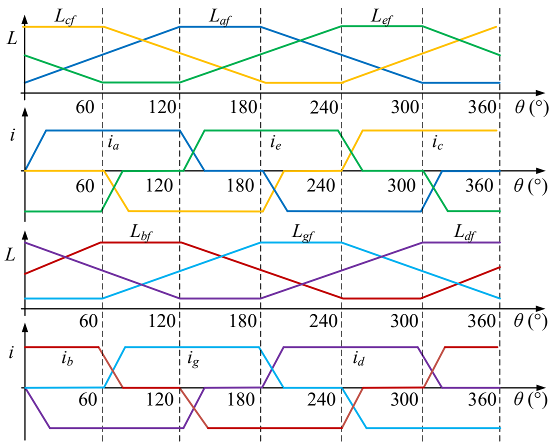

Fig. 12. Conduction mode of 12/10 DC-VRM.

B. Determination of Detection Pulse Width

When the test pulse of phase A is injected, the response current can be expressed as

$$I_a=\frac{U_{dc}}{R}(1\text{-}e^{-\frac{\Delta t}{\tau_a}}) \tag{13}$$

where $\tau_a=\frac{L_a}{R}$ is the time constant of the detection pulse injected into the equivalent circuit. The response current will increase with the increase of the conduction time, which causes the increase of electromagnetic torque. When the electromagnetic torque is greater than the load torque, the motor rotates. This may affect the detection accuracy and even cause the motor to reverse. To avoid this phenomenon, the detection pulse width needs to be restricted to a certain range. During the pulse injection stage, the influences of mutual inductance between sub-phases are avoided by H-bridge drive sequentially conduction. T_{am} can also be ignored, the maximum torque generated by the detection pulse can be expressed as

$$T_{max}=I_a i_f\frac{dL_{af}}{d\theta}+\frac{1}{2}I_a^2\frac{dL_a}{d\theta} \tag{14}$$

For a certain field winding current and a sub-phase winding current, the torque production is decided by the electrical sector. For example, in sectors III and VI, both L_{af} and L_a are in the flat top or flat bottom area, so in these areas, the inductance slope is small, and torque generated is also limited. It is known from the above analysis that the mutual inductance between the field winding and sub-phase has high linearity in the rising and falling stages. Assume that the slops of the sub-phase self-inductance changing relative to the rotor position during the rising and falling stages are k and $-k$, respectively. Then the slop of L_{af} during the rising and falling stages can be expressed as nk and $-nk$, respectively. Assume that the motor load torque is T_l, the equation (11) needs to be met to prevent the motor from

This article has been accepted for publication in a future issue of this journal, but has not been fully edited. Content may change prior to final publication. Citation information: DOI 10.1109/TEC.2022.3167551, IEEE Transactions on Energy Conversion

rotating during the position detection period.

$$T_{max}<T_l \tag{15}$$

Therefore, bring the formula (8), (9) and (10) into (11),

$$\frac{U_{dc}}{R}(1-e^{-\frac{\Delta t}{\tau_a}})<\frac{\sqrt{4n^2k^2i_f^2+8kT_l}-2nki_f}{2k} \tag{16}$$

The detection pulse injection width can be limited to

$$\Delta t<\frac{L_{min}}{R}\ln\frac{2kU_{dc}}{2kU_{dc}+2nki_fR-R\sqrt{4n^2k^2i_f^2+8kT_l}} \tag{17}$$

In addition, the detection pulse width should be wide enough to be detected. If the detection pulse width is too small, it may cause the response current cannot be detected, affect the accuracy of position judgment, and lead to commutation errors. The peak response current should be greater than the minimum current i_{min} value that can be detected by the current sensor

$$\frac{U_{dc}}{R}\left(1-e^{-\frac{\Delta t}{\tau_a}}\right)\ge i_{min} \tag{18}$$

Finally, the width of the detection pulse can be selected within this range

$$\frac{L_{max}}{R}\ln\frac{U_{dc}}{U_{dc}-Ri_{min}}\le\Delta t<\frac{L_{min}}{R}\ln\frac{2kU_{dc}}{2kU_{dc}+2nki_fR-R\sqrt{4n^2k^2i_f^2+8kT_l}} \tag{19}$$

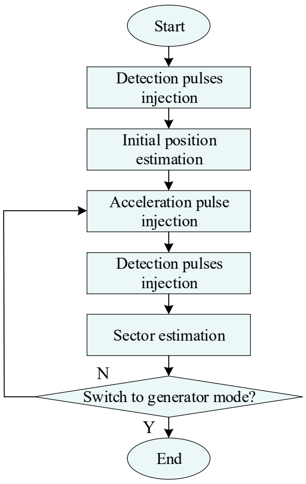

Fig. 13. Flowchart of sensorless startup for 12/10 DC-VRM.

C. Sensorless Operation as ISG

Fig. 13 shows the implementation of reconstructing saliency sensorless startup of 12/10 DC-VRM. DC-VRM should be driven by the proposed reconstructing saliency method to achieve pulse injection self-inductance detection. First, the detection pulses are injected into each sub-phase in turn by H-bridge converters. Then by comparing the magnitudes of the response current peaks, the estimated sector position is determined. The acceleration pulses and the detection pulses are injected in sequence for acceleration and self-inductance detection, respectively. In this way, the speed of the machine can increase steadily. Once the machine is operated in generator mode, the induced voltage can be collected by H-bridge converters independently.

V. Experimental Results

A. Experimental Setup

The experiments are carried out to verify the effectiveness of the proposed parallel sensorless drive system. The 12/10 DC-VRM prototype is fabricated. The rotor lamination, stator lamination, and assembly are shown in Fig. 14(a). (b). (c), respectively. The experimental setup is shown in Fig .14(d). The sensorless control is performed based on a real-time control platform of a dSPACE MicroLabBox with a sampling rate of 50kHz. The control parameters can be set and modified by Controldesk. The DC-VRM is driven by commercial H-bridge converters which are excited by the DC source. Another DC source is applied to the field winding to establish the excitation magnetic field. A coaxial magnetic powder brake is connected to the motor to provide load torque. The actual rotor position is acquired by a resolver to compare with the position acquired by the detection method.

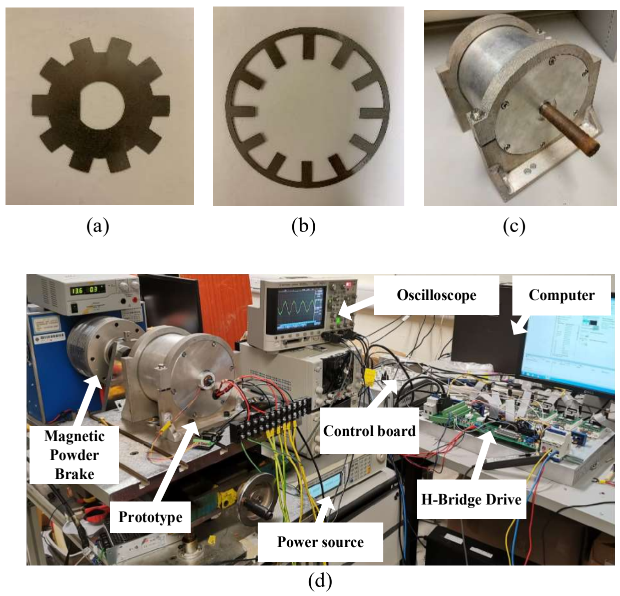

Fig. 14. The prototype and test bench setup. (a) Rotor core lamination (b) Stator core lamination (c) Assembly of the prototype. (d) Test bench setup.

B. Saliency Annihilation and Reconstructing

The electromagnetic characteristics of the DC-VRM prototype are firstly tested. Fig .15 (a) shows the back-EMFs of U, V, W windings, while those of the sub-phases are given in Fig .15 (b). Although there are some voltage distortions in sub-phases, the synthetic back-EMFs are symmetrical and balanced. The saliency annihilation phenomenon and the reconstructing saliency effect by parallel H-bridge converter are shown in Fig .16. The measured self-inductances of U, V, W windings, as well as sub-phase A, C, D and E agree well with those from the finite element analysis. It is proved that the synthetic

This article has been accepted for publication in a future issue of this journal, but has not been fully edited. Content may change prior to final publication. Citation information: DOI 10.1109/TEC.2022.3167551, IEEE Transactions on Energy Conversion

saliency is obliterated, while that in sub-phases is still distinct, as the sub-phase self-inductances change periodically with rotor position. This enables the low-speed sensorless operation for the proposed DC-VRM drive system using self-inductance detection-based rotor position estimation methods.

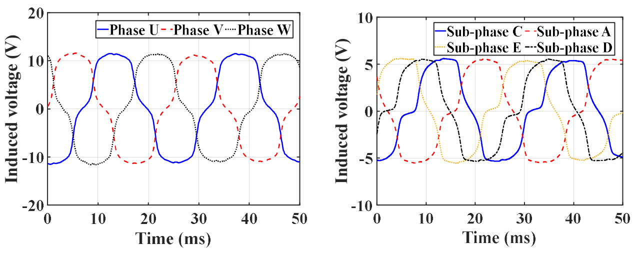

Fig. 15. (a) Back-EMFs of phase U, V and W. (b) Sub-phase back-EMFs.

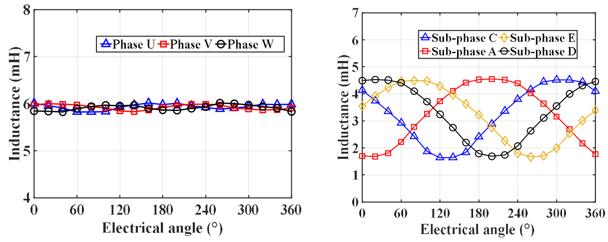

Fig. 16. (a) Self-inductances of phases U, V and W under traditional winding connections. (b) Self-inductances of sub-phases through the proposed reconstructing saliency effect.

C. Initial Position Detection

To verify the initial position detection ability by the proposed sensorless drive, the rotor of the machine is manually located at different initial positions for detection. The measured results are presented in Fig. 17, including the sub-phase current with pulse injection, practical rotor sector information obtained by sensors, and the estimated positions. By injecting the detection pulses in sequence, the peak values of the resultant currents are not influenced by mutual inductance, thus keeping the detection accuracy in initial position detection. These resultant currents are collected and compared in dSPACE MicroLabBox to determine the sector information. As shown in Fig. 17(a) to Fig. 17(f), the information on the initial sector position can be accurately obtained by comparing the amplitudes of the resultant currents in the whole six sectors.

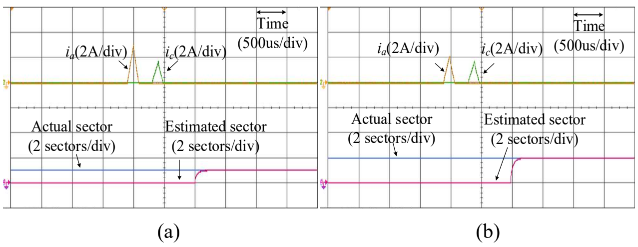

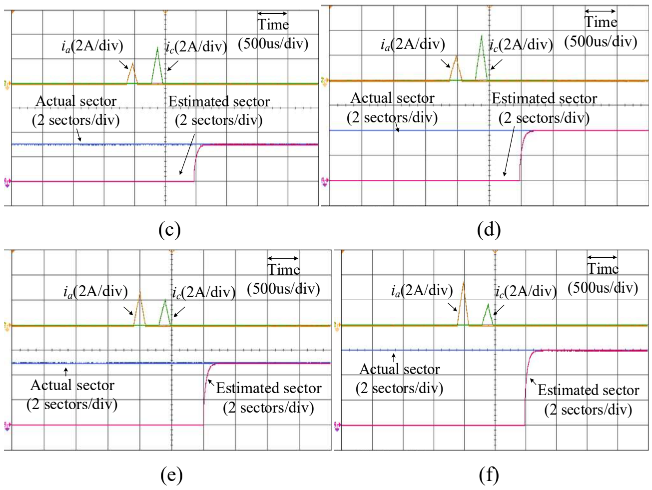

Fig. 17. Initial position estimation in whole sectors. (a) Sector I. (b) Sector II. (c) Sector III. (d) Sector IV. (e) Sector V. (f) Sector VI.

D. Position Estimation during the Free-running Stage

Fig .18 shows the sector estimation results during the free-running stage. After the motor is accelerated to a certain speed, the injection of acceleration pulses is stopped, and the motor continues to rotate due to inertia. In this stage, the detection pulses are still injected to acquire the rotor position. It is clear to see that a reliable position still can be acquired during the free-running stage.

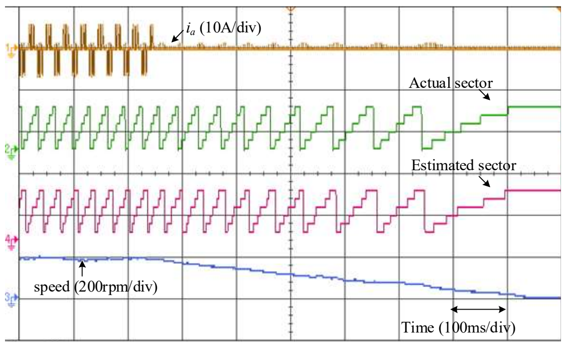

Fig. 18. Position estimation during the free-running stage.

E. Sensorless Acceleration

Fig .19 shows the whole process of the initial detection and acceleration stage with the proposed sensorless drive system. At first, detection pulses are injected to estimate the initial rotor position. The widths of the detection pulse and the acceleration pulse are designed as 0.1ms and 2ms, respectively. Due to the injection of short pulses in this startup method, additional filters are not required. Therefore, there is no significant difference in phase between the estimated sector and the actual sector. In addition, the sector estimation can be precisely acquired in the whole six sectors, which corresponds to 6° in each sector. Then, with the alternate injection of detection pulses and acceleration pulses, the rotor speed gradually increases. The rotor speed can reach the determined speed of 200rpm in one second. In generator mode, the back-EMF can be collected for energy recycling.

This article has been accepted for publication in a future issue of this journal, but has not been fully edited. Content may change prior to final publication. Citation information: DOI 10.1109/TEC.2022.3167551, IEEE Transactions on Energy Conversion

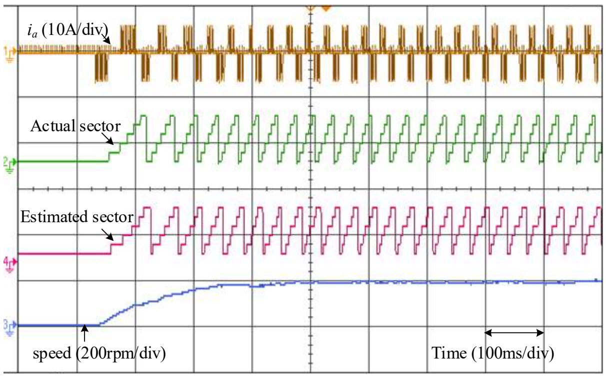

Fig. 19. Sensorless control acceleration for 12/10 DC-VRM.

F. Analysis of torque performance

The torque performance during the startup process is shown in Fig .20. As the torque generation is mainly composed of acceleration pulses, the torque generated by the detection pulses can be overlooked. The torque curve fluctuates from 0Nm to 5Nm. However, the average torque can keep constant in the start-up stage, thus guaranteeing the start-up performance.

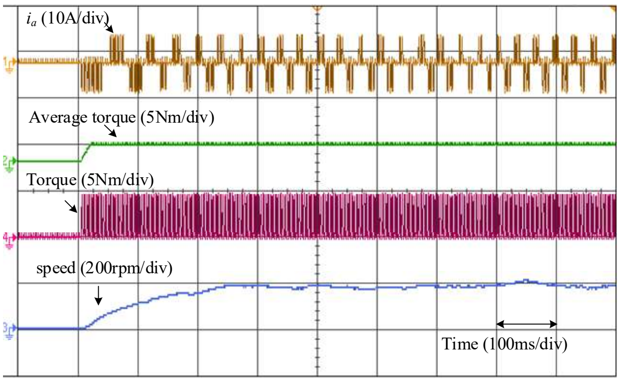

Fig. 20. Torque generation during the start-up process.

CONCLUSION

This paper analyzed the saliency annihilation phenomenon in 12/10 DC-VRM driven by a traditional three-phase inverter from the perspective of sensorless drive for the first time. Self-inductance odd-order harmonics including the fundamental component are canceled by the 12/10 pole combination. This phenomenon has been illustrated through Fourier analysis, finite element analysis and experiments, respectively. To achieve the self-inductance tracking sensorless drive, a reconstructing saliency method for 12/10 DC-VRM sensorless drive is proposed to recover the saliency in self-inductance. By using a parallel H-bridge drive system, the constant phase inductance can be split into two variable inductance components having opposite trends, thereby advanced position estimation method based on inductances detection can be applied. In addition, due to the independent current control feature using the parallel drive, a sequential pulse injection method can be applied to estimate the rotor position with high accuracy and high robustness, while avoiding the influence of mutual inductances between phases. The experimental results prove the effectiveness of the proposed parallel sensorless drive for DC-VRM during initial position detection, start-up and free-running stages. A sector estimation accurate to 6° can be achieved. In general, the proposed solution can combine the advantages of inherent low torque ripple of 12/10 DC-VRM and high-accuracy sensorless operation, thus boosting the system robustness with reduced noise and eliminated position sensor. Its good fault-tolerant ability can be applied in safety-critical industry applications such as aerospace propulsion. It should be admitted using a parallel H-bridge drive will increase the number of power switches and system costs. Future research will develop a method to balance the system cost.

REFERENCES

[1] A. Griffo, R. Wrobel, P. H. Mellor and J. M. Yon, "Design and Characterization of a Three-Phase Brushless Exciter for Aircraft Starter/Generator," *IEEE Trans Ind. Appl.,* vol. 49, no. 5, pp. 2106-2115, Sept.-Oct. 2013.

[2] R. Bojoi, A. Cavagnino, A. Tenconi and S. Vaschetto, "Control of Shaft-Line-Embedded Multiphase Starter/Generator for Aero-Engine," *IEEE Trans. Ind. Electron*., vol. 63, no. 1, pp. 641-652, Jan. 2016.

[3] N. Jiao, C. Sun, X. Zhang, X. Duan and W. Liu, "Double-Side Voltage-Behind-Reactance Model of Brushless Exciter in Aircraft Wound-Rotor Synchronous Starter-Generator Considering Magnetic Saturation," *IEEE Trans. Energy Convers.*, vol. 36, no. 3, pp. 2358-2369, Sept. 2021.

[4] P. B. Reddy, A. M. El-Refaie, K. K. Huh, J. K. Tangudu and T. M. Jahns, "Comparison of interior and surface PM machines equipped with fractional-slot concentrated windings for hybrid traction applications," IEEE Trans. Energy Convers., vol. 27, no. 3, pp. 593-602, Sept. 2012.

[5] M. Cheng, W. Hua, J. Zhang and W. Zhao, "Overview of Stator-Permanent Magnet Brushless Machines," *IEEE Trans. Ind. Electron*., vol. 58, no. 11, pp. 5087-5101, Nov. 2011.

[6] I. Boldea, L. N. Tutelea, and D. Dorrell, "Automotive electric propulsion systems with reduced or no permanent magnets: an overview," *IEEE Trans. Ind. Electron*., vol. 61, no. 10, pp. 5696-5711, Oct. 2014.

[7] X. Zhao, S. Niu, and W. Fu, "Design of a new relieving-DC-saturation hybrid reluctance machine for fault-tolerant in-wheel direct drive," *IEEE Trans. Ind. Electron*., vol. 67, no. 11, pp. 9571-9581, Nov. 2020.

[8] D. Xiao, J. Ye, G. Fang, Z. Xia, X. Wang and A. Emadi, "Improved feature-position-based sensorless control scheme for SRM drives based on nonlinear state observer at medium and high speeds," *IEEE Trans. Power Electron*., vol. 36, no. 5, pp. 5711-5723, May 2021.

[9] X. D. Xue, K. W. E. Cheng and S. L. Ho, "Optimization and evaluation of torque-sharing functions for torque ripple minimization in switched reluctance motor drives," *IEEE Trans. Power Electron*., vol. 24, no. 9, pp. 2076-2090, Sept. 2009.

[10] R. Martin, J. D. Widmer, B. C. Mecrow, A. Mebarki and N. L. Brown, "Electromagnetic considerations for a six-phase switched reluctance motor driven by a three-phase inverter," *IEEE Trans. Ind. Appl*., vol. 52, no. 5, pp. 3783-3791, Sep. 2016.

[11] S. Ullah, S. P. McDonald, R. Martin, M. Benarous and G. J. Atkinson, "A permanent magnet assist, segmented rotor, switched reluctance drive for fault tolerant aerospace applications," *IEEE Trans Ind. Appl.,* vol. 55, no. 1, pp. 298-305, Jan.-Feb. 2019.

[12] Y. Jin, B. Bilgin, and A. Emadi, "An extended-speed low-ripple torque control of switched reluctance motor drives," *IEEE Trans. Power Electronics*, vol. 30, pp. 1457-1470, 2015.

[13] C. Gan, J. Wu, Q. Sun, W. Kong, H. Li and Y. Hu, "A review on machine topologies and control techniques for low-noise switched reluctance motors in electric vehicle applications," *IEEE Access*, vol. 6, pp. 31430-31443, 2018.

[14] L. Yu, Z. Zhang, Z. Chen and Y. Yan, "Analysis and verification of the doubly salient brushless DC generator for automobile auxiliary power unit

application," *IEEE Trans Ind. Electron*., vol. 61, no. 12, pp. 6655-6663, Dec. 2014.

[15] Z. Chen, and Y. Yan "A doubly salient starter/generator with two section twisted-rotor structure for potential future aerospace application," *IEEE Trans. Ind. Electron*., vol. 59, no. 9, pp. 3588- 3595, Sept. 2012

[16] X. Liu and Z. Q. Zhu, "Stator rotor pole combinations and winding configurations of variable flux reluctance machines," *IEEE Trans. Ind. Appl*., vol. 50, no. 6, pp. 3675-3684, Nov.-Dec. 2014.

[17] L. R. Huang, J. H. Feng, S. Y. Guo, J. X. Shi, W. Q. Chu and Z. Q. Zhu, "Analysis of torque production in variable flux reluctance machines," in *IEEE Trans. Energy Convers*, vol. 32, no. 4, pp. 1297-1308, Dec. 2017.

[18] S. Jia, R. Qu, J. Li, D. Li and H. Lu, "Design considerations of stator DC-winding excited vernier reluctance machines based on the magnetic gear effect," *IEEE Trans. Ind. Appl*., vol. 53, no. 2, pp. 1028-1037, March-April 2017.

[19] X. Zhao and S. Niu, "Design and optimization of a novel slot-PM-assisted variable flux reluctance generator for hybrid electric vehicles," *IEEE Trans. Energy Convers.*, vol. 33, no. 4, pp. 2102-2111, Dec. 2018.

[20] X. Zhao, S. Niu, X. Zhang and W. Fu, "Flux-Modulated Relieving-DC-Saturation Hybrid Reluctance Machine With Synthetic Slot-PM Excitation for Electric Vehicle In-Wheel Propulsion," *IEEE Trans Ind. Electron*., vol. 68, no. 7, pp. 6075-6086, July 2021.

[21] X. Zhao, S. Wang, S. Niu, W. Fu and X. Zhang, "A Novel High-Order-Harmonic Winding Design Method for Vernier Reluctance Machine With DC Coils Across Two Stator Teeth," *IEEE Trans Ind. Electron*., vol. 69, no. 8, pp. 7696-7707, Aug. 2022.

[22] M. Abdelrahem, C. M. Hackl, R. Kennel and J. Rodríguez, "Computationally Efficient Finite-Position-Set-Phase-Locked Loop for Sensorless Control of PMSGs in Wind Turbine Applications," *IEEE Trans. Power Electron.*, vol. 36, no. 3, pp. 3007-3016, March 2021.

[23] R. Sreejith and B. Singh, "Sensorless Predictive Current Control of PMSM EV Drive Using DSOGI-FLL Based Sliding Mode Observer," *IEEE Trans. Ind. Electron*., vol. 68, no. 7, pp. 5537-5547, July 2021.

[24] G. Liu, X. Chen, X. Zhou and S. Zheng, "Sensorless Commutation Deviation Correction of Brushless DC Motor with Three-Phase Asymmetric Back-EMF," *IEEE Trans Ind. Electron*., vol. 67, no. 7, pp. 6158-6167, July 2020.

[25] Hongwei Gao, F. R. Salmasi and M. Ehsani, "Inductance model-based sensorless control of switched reluctance motor drive at low speed," *IEEE Trans. Power Electron.*, vol. 19, no. 6, pp. 1568-1573, Nov. 2004.

[26] J. Cai and Z. Deng, "Unbalanced Phase Inductance Adaptable Rotor Position Sensorless Scheme for Switched Reluctance Motor," *IEEE Trans. Power Electron.*, vol. 33, no. 5, pp. 4285-4292, May 2018.

[27] M. Krishnamurthy, C. S. Edrington and B. Fahimi, "Prediction of rotor position at standstill and rotating shaft conditions in switched reluctance machines," *IEEE Trans. Power Electron.*, vol. 21, no. 1, pp. 225-233, Jan. 2006.

[28] A. Khalil et al., "Four-Quadrant Pulse Injection and Sliding-Mode-Observer-Based Sensorless Operation of a Switched Reluctance Machine Over Entire Speed Range Including Zero Speed," *IEEE Trans. Ind. Appl*., vol. 43, no. 3, pp. 714-723, May-june 2007.

[29] G. Pasquesoone, R. Mikail and I. Husain, "Position Estimation at Starting and Lower Speed in Three-Phase Switched Reluctance Machines Using Pulse Injection and Two Thresholds," *IEEE Trans. Ind. Appl*., vol. 47, no. 4, pp. 1724-1731, July-Aug. 2011.

[30] L. Shen, J. Wu and S. Yang, "Initial Position Estimation in SRM Using Bootstrap Circuit Without Predefined Inductance Parameters," *IEEE Trans. Power Electron.*, vol. 26, no. 9, pp. 2449-2456, Sept. 2011.

[31] Moradi, Hassan, and Ebrahim Afjei. "Novel rotor position estimation technique for switched reluctance motor (SRM)." *Int. J. Electron.*, no. 9 (2011): 1169-1184

[32] H. M. CheshmehBeigi, "Design and Implementation of the New Sensorless Rotor Position Estimation in Homopolar Salient-Pole Brushless DC Motor," *IEEE J. Emerg. Sel. Topics Power Electron*., doi: 10.1109/JESTPE.2019.2944294.

[33] J. Cai and Z. Liu, "An Unsaturated Inductance Reconstruction Based Universal Sensorless Starting Control Scheme for SRM Drives," *IEEE Trans. Ind. Electron*., vol. 67, no. 11, pp. 9083-9092, Nov. 2020.

[34] X. Zhou, B. Zhou, J. Yu, L. Yang and Y. Yang, "Research on Initial Rotor Position Estimation and Anti-Reverse Startup Methods for DSEM," *IEEE Trans. Ind. Electron*., vol. 64, no. 4, pp. 3297-3307, April 2017.

[35] X. Zhou, B. Zhou and K. Wang, "Position Sensorless Control for Doubly Salient Electromagnetic Machine with Improved Startup Performance," *IEEE Trans. Ind. Electron*., vol. 67, no. 3, pp. 1782-1791, March 2020.

XING ZHAO (Member, IEEE) received the B.Eng. degree from Nanjing University of Aeronautics and Astronautics, Nanjing, China, in 2014, and the Ph.D. degree from The Hong Kong Polytechnic University, Hong Kong, China, in 2020, both in Electrical Engineering.

From Jul. 2019 to Jan. 2020, he was a Visiting Research Scholar with the Center for Advanced Power Systems, Florida State University, Tallahassee, USA. Between Jul. 2020 and Oct. 2021, he served as a Research Assistant Professor with the Department of Electrical Engineering, The Hong Kong Polytechnic University. Since Nov. 2021, he has been a Lecturer in the Department of Electronic Engineering with University of York, UK. He has authored or coauthored more than 50 technical papers in the international journals and conferences and holds six granted patents. His research interests include advanced electrical machines, motor drives, and power electronics for electric vehicles and renewable energy systems.

WEIYU WANG is currently working toward the Ph.D. degree in electrical engineering with the Department of Electrical Engineering, Hong Kong Polytechnic University, Hong Kong, China.

His research interests include electrical machine drive and position-sensorless drive.

SHUANGXIA NIU (Sennior Member, IEEE) received the B.Sc. and M.Sc. degrees in electrical engineering from the School of Electrical Engineering and Automation, Tianjin University, Tianjin, China, in 2002 and 2005, respectively, and the Ph.D. degree in electrical engineering from the Department of Electrical and Electronic Engineering, The University of Hong Kong, Hong Kong, in 2009, all in electrical engineering.

Since 2009, she has been with The Hong Kong Polytechnic University, Hong Kong, where she is currently an Associate Professor with the Department of Electrical Engineering. She has authored or coauthored over 100 articles in leading journals. Her research interests include novel electrical machines and drives, renewable energy conversion systems, and applied electromagnetics.

WEINONG FU obtained his PhD from The Hong Kong Polytechnic University (PolyU) in 1999. He is a Professor at Shenzhen Institutes of Advanced Technology, Chinese Academy of Sciences. He worked at PolyU about 13 years as an Associate Professor and full Professor. He was one of the key developers at Ansoft Corporation in Pittsburgh, USA. He has about seven years of working experience at Ansoft, focusing on the development of commercial software Maxwell®, which is a leading commercial software package for the computation of electromagnetic fields of electromechanical equipments. During 1982 to 1986, he worked at *Shanghai Electrical Apparatus Research Institute*, where he accumulated valuable experience to deal with the design and manufacturing of electric devices in practice, and constructed a solid foundation for further academic career development. Prof. Fu has made many contributions to the theory and application of electromagnetic field computation and electric device design, including the publication of over 250 refereed journal papers. He regularly serves as paper reviewer for *IEEE Trans. Magnetics*, *IEEE Trans. Energy Conversion, IEEE Trans. Industrial Electronics*, *IEEE Trans. Power Electronics, IEEE Trans. Industry Application*, *Energies,* and *COMPUMAG*, *CEFC*, *INTERMAG* international conferences. Prof. Fu's research interests mainly focus on computational electromagnetics, optimal design of electric devices, applied electromagnetics, and novel electric machines.